Advanced Functional Materials

ADVANCED FUNCTIONAL MATERIALS
www.afm-journal.de

RESEARCH ARTICLE

Steering Dynamic Surface Reconstruction via Octahedral Stacking: A Strategy for Highly Efficient Hydrogen Evolution

Ning Sun[1,2] | Bowen Zhang[2] | Yuwei Liu[3,4] | Yang Qin[5] | Xinyu Xie[1] | Guowei Liu[1] | Pengda Ye[3,4] | Xiangjiang Dong[2] | Gongjin Xu[2] | Lei Lian[2] | Peng Wei[2] | Lijia Zhou[2] | Yu-Cheng Huang[6] | Jing Zhou[7] | Jihao Zhang[8] | Ruxanda Mireanu[8] | Qingyu Kong[8] | Ying-Rui Lu[9] | Zhiwei Hu[10] | Ming Lei[5] | Kai Huang[1] | Xiang Li[3,4] | Runze Yu[2]

[1]State Key Laboratory of Information Photonics and Optical Communications, School of Physical Science and Technology, Beijing University of Posts and Telecommunications, Beijing, P. R. China | [2]Center For High Pressure Science and Technology Advanced Research, Beijing, P. R. China | [3]Centre For Quantum Physics, Key Laboratory of Advanced Optoelectronic Quantum Architecture and Measurement (MOE), School of Physics, Beijing Institute of Technology, Beijing, P. R. China | [4]Beijing Key Lab of Nanophotonics & Ultrafine Optoelectronic Systems, School of Physics, Beijing Institute of Technology, Beijing, P. R. China | [5]State Key Laboratory of Information Photonics and Optical Communications, School of Integrated Circuits, Beijing University of Posts and Telecommunications, Beijing, P. R. China | [6]Curtin Centre for Advanced Energy Materials and Technologies (CAEMT), Western Australian School of Mines (WASM), Curtin University, Perth, Western Australia, Australia | [7]Zhejiang Institute of Photoelectronics & Zhejiang Institute for Advanced Light Source, Zhejiang Normal University, Jinhua, Zhejiang, P. R. China | [8]Synchrotron Soleil L'Orme des Merisiers, St-Aubin, France | [9]National Synchrotron Radiation Research Center, Hsinchu, Taiwan | [10]Max Planck Institute for Chemical Physics of Solids, Dresden, Germany

Correspondence: Kai Huang (huang-kai@bupt.edu.cn) | Xiang Li (xiangli@bit.edu.cn) | Runze Yu (runze.yu@hpstar.ac.cn)

Received: 30 December 2025 | **Revised:** 4 March 2026 | **Accepted:** 17 March 2026

Keywords: alkaline hydrogen evolution reaction | $BaRuO_3$ perovskites | in situ Raman spectroscopy | octahedral connectivity | surface reconstruction

ABSTRACT

Surface reconstruction governs the activity and stability of oxide-based electrocatalysts in alkaline hydrogen evolution reaction (HER), yet its structural origins remain unclear. Here, we show that tuning the connectivity of RuO_6 octahedra in $BaRuO_3$ perovskites modulates reconstruction thermodynamics, with the balance between corner- and face-sharing units determining the formation of amorphous surface Ru_xO_y layers. Increased corner-sharing weakens lattice cohesion and promotes early Ba/Ru dissolution and amorphization, whereas excessive face-sharing suppresses reconstruction. The 6H phase, featuring a balanced connectivity motif, undergoes moderate, self-activating reconstruction that preserves bulk stability. In situ Raman spectroscopy reveals rapid Ru–O rearrangement producing an amorphous Ru_xO_y shell with accelerated OH* turnover and interfacial water reorganization. Density functional theory (DFT) shows that reconstructed Ru_xO_y domains redistribute interfacial charge, strengthen Ru 4*d*–O 2*p* orbital hybridization, lower the water-dissociation barrier, and optimize hydrogen-binding energetics. These features account for the outstanding performance of AC-6H (the activated 6H-$BaRuO_3$ is denoted as AC-6H), achieving 11 mV at 10 mA cm^{-2} and sustaining 150 h at 200 mA cm^{-2}. This work establishes octahedral-connectivity engineering as a platform for directing reconstruction and designing high-performance HER catalysts.

Ning Sun, Bowen Zhang, and Yuwei Liu contributed equally to this work.

1 | Introduction

The physical and chemical properties of functional materials are fundamentally governed by the connectivity of their basic structural units [1]. In transition-metal oxides and related covalent or ionic solids, these units are predominantly octahedrally coordinated [2, 3]. From a polytypism perspective, variations in corner-, edge-, or face-sharing of octahedra can generate multiple crystalline polytypes at identical compositions, reflecting a competition among metal–metal interactions, lattice packing efficiency, and free-energy minimization [4]. Importantly, octahedral stacking simultaneously defines local coordination geometry, metal–metal separation, and framework density, rendering the relative stability of different polytypes highly sensitive to lattice chemistry and external pressure. The 3C, 4H, 6H, and 9R phases exemplify this structural diversity, arising from distinct stacking sequences of octahedra along close-packed directions and giving rise to cubic ($Pm\bar{3}m$), hexagonal ($P63/mmc$), and rhombohedral ($R\bar{3}m$) symmetries [5]. Such connectivity-driven structural variations regulate metal–metal coupling, electronic delocalization, and lattice strain, thereby reshaping the electronic structure and orbital configuration [6]. In particular, reduced metal–metal distances associated with higher-order octahedral sharing enhance *d*–*d* and *d*–*p* orbital hybridization, reorganizing electronic states near the Fermi level and modulating binding strength of reaction intermediates during catalysis [7]. Moreover, the shortened metal-metal distance from corner- to edge-sharing configurations is expected to accelerate catalytic kinetics by minimizing repulsion and optimizing reaction pathways. Consequently, octahedral-stacking engineering has emerged as an effective strategy for interrogating catalytic mechanisms, while elucidating how distinct stacking motifs govern dynamic surface reconstruction remains a critical challenge [8].

Electrocatalytic hydrogen production is central to renewable-energy conversion, and anion-exchange membrane water electrolysis (AEMWE) has become a promising platform for large-scale H_2 generation [9, 10]. However, the hydrogen evolution reaction (HER) in alkaline media is intrinsically limited by sluggish water dissociation and the low availability of protons at the catalyst surface [11]. In the Volmer step of alkaline HER, H* species are generated through water dissociation ($H_2O + e^- \rightarrow H^* + OH^-$), which imposes an additional energy barrier and limits the reaction rate [12]. Ruthenium, costing only a quarter of platinum, demonstrates comparable or even superior alkaline HER activity due to its high oxygen affinity and low energy barrier for H_2O dissociation [13, 14]. However, Ru-based catalysts remain constrained by slow water dissociation with inadequate proton supply, suboptimal H* adsorption/desorption, and evolving surface structures during operation. Surface reconstruction is especially pronounced for Ru, which often forms amorphous Ru_xO_y or Ru clusters during alkaline HER [15], accompanied by notable elemental dissolution that obscures the identity of the true active phase and compromises durability [16]. In addition, the reconstructed interface continuously exchanges atoms and intermediates, generating new surface species while erasing others [17], complicating mechanistic interpretation. Therefore, a well-defined Ru-based platform is needed to elucidate how reconstruction layers form, evolve, and interact with intermediates, and how these processes determine catalytic activity and stability.

By manipulating the configuration of RuO_6 octahedra from corner- to face-sharing, one can probe how connectivity governs alkaline HER kinetics; however, such investigations remain limited due to synthetic challenges and the absence of in situ mechanistic insight. Here, we introduce a connectivity-guided self-activation strategy in which the ratio of corner- and face-sharing RuO_6 units in $BaRuO_3$ is systematically tuned to regulate surface reconstruction during alkaline HER. Reduced corner-sharing structures enhance bulk stability but suppress reconstruction, whereas increased corner-sharing structures facilitate lattice reorganization and boost catalytic activity (Scheme 1). The 6H phase achieves an optimal balance, preserving structural integrity while enabling controlled surface reconfiguration. In situ Raman spectroscopy reveals rapid formation of amorphous surface Ru_xO_y on 6H-$BaRuO_3$ (AC-6H; the activated sample is denoted as AC-sample), accompanied by accelerated intermediate turnover and reorganization of interfacial water. Density functional theory (DFT) shows that reconstructed Ru_xO_y domains trigger interfacial charge redistribution, strengthen Ru–O 4*d*–2*p* orbital hybridization, thereby lowering the water-dissociation barrier and tuning hydrogen-adsorption energetics. These refinements collectively explain the high HER performance of AC-6H, which requires only 11 mV at 10 mA cm^{-2} and maintains stability for over 150 h at 200 mA cm^{-2} in 1.0 M KOH. Overall, this work establishes octahedral-connectivity engineering as an effective strategy for controlling reconstruction and developing durable alkaline HER catalysts.

2 | Results and Discussion

2.1 | Synthesis and Structural Characterization

$BaRuO_3$ perovskites with different crystalline phases were synthesized using two established routes: the 9R phase via a solid-state method, and the 4H, 6H, and 3C phases via a previously reported high-pressure high-temperature (HPHT) procedure [18]. Powder x-ray diffraction (PXRD) refinements confirm that all samples are phase-pure without detectable impurities (Figure S1). Notably, $BaRuO_3$ exhibits four structural configurations derived from different combinations of Ru–O octahedra and basic building units, including Ru_2O_9 dimers and Ru_3O_{12} trimers, which involve various face-sharing and corner-sharing connection modes (Figure S2). This structural diversity provides an ideal platform to probe how RuO_6 connectivity dictates lattice stability and reconstruction propensity. Specifically, 9R-$BaRuO_3$ ($R\bar{3}m$) consists of face-sharing Ru_3O_{12} trimers linked by corner-sharing oxygen atoms, while 4H-$BaRuO_3$ ($P6_3/mmc$) contains face-sharing Ru_2O_9 dimers connected through corner-sharing oxygens. 6H-$BaRuO_3$ ($P6_3/mmc$) features both Ru_2O_9 dimers and RuO_6 octahedra joined by corner-sharing oxygen atoms, whereas 3C-$BaRuO_3$ ($Pm\bar{3}m$) is composed exclusively of corner-shared RuO_6 octahedra. Scanning electron microscopy (SEM) and transmission electron microscopy (TEM) images reveal that the sample consists of micrometer-sized particles (Figures S3–S7). High-resolution TEM (HR-TEM) and the corresponding selected-area electron diffraction (SAED) pattern confirm clear lattice fringes and single-crystal characteristics for the $BaRuO_3$ family. Energy-dispersive spectroscopy (EDS) mapping confirms a homogeneous Ba, Ru, and O distribution at an approximate ratio of 1:1:3 (Figure S8). These results verify the successful preparation

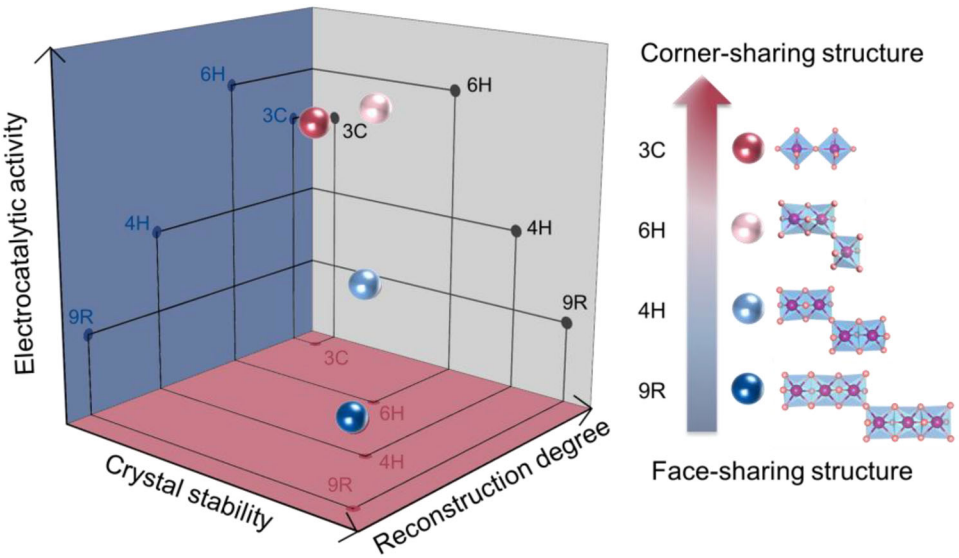

SCHEME 1 | Schematic diagram linking crystal stability, reconstruction degree, and electrocatalytic activity along the transition from corner- to face-sharing RuO_6 frameworks.

of phase-pure samples and provide a solid basis for investigating their dynamic structural evolution during electrocatalysis.

Perovskite oxides frequently undergo elemental leaching and surface reconstruction during electrocatalysis—a process often described as "activation." Following common practice [19, 20], the $BaRuO_3$ samples were activated by linear sweep voltammetry (LSV) over 1, 35, and 50 cycles and subsequently characterized. Ex situ XRD (Figure S9) reveals the formation of a $Ba(OH)_2{\cdot}8H_2O$ secondary phase in all $BaRuO_3$ polymorphs except 6H-$BaRuO_3$, consistent with its superior structural robustness [21]. HR-TEM analysis (Figure S10) reveals that 9R-, 4H-, and 3C-$BaRuO_3$ rapidly form amorphous surface layers with embedded nanoclusters after only one LSV cycle, whereas 6H-$BaRuO_3$ develops a predominantly amorphous surface without obvious clustering. This reconstruction behavior is consistent with recent reports by Wang et al., who demonstrated bias-driven dynamic surface reconstruction and Ru cluster formation in mixed-phase 9R/6H-$BaRuO_3$ [22]. Combining PXRD results, our data further indicate that surface Ru species originate from Ba-induced lattice destabilization, establishing Ba dissolution as the primary trigger for Ru reconstruction. Upon prolonged activation (50 LSV cycles), a distinct phase-dependent evolution is observed. Notably, no discernible clusters are detected on any sample. In contrast, pronounced differences in amorphous layer thickness emerge: 9R-, 4H-, and 6H-$BaRuO_3$ retain relatively thin amorphous layers of 7.4, 8.7, and 4.8 nm, respectively, whereas 3C-$BaRuO_3$ undergoes severe amorphization, reaching a thickness of ~70.7 nm (Figure S11). Moreover, this evolution correlates strongly with the Ru—O bond length and octahedral connectivity (Figure S12). In the hexagonal polytypes, elongated Ru—O bonds may enhance lattice flexibility and strain accommodation, thereby suppressing amorphous layer growth. By contrast, cubic 3C-$BaRuO_3$, despite its longest Ru—O bond, possesses a rigid fully corner-sharing RuO_6 framework that is intrinsically unstable under HER conditions, leading to catastrophic amorphization. Inductively coupled plasma optical emission spectroscopy (ICP-OES) measurements (Table S1) reveal that the dissolution of both Ba and Ru generally decreases with increasing fractions of corner-sharing octahedra. Notably, the 6H phase, which possesses a balanced ratio of corner- and face-sharing RuO_6 units, exhibits the lowest Ru dissolution, likely accounting for its superior catalytic stability. Interestingly, Ru dissolution shows a strong positive correlation with the Ru—O bond length, with longer Ru—O bonds leading to accelerated Ru leaching (Figure S13). Consistently, 6H-$BaRuO_3$ features the shortest Ru—O bond length and correspondingly the lowest Ru dissolution rate, underscoring the critical role of local bonding environments in governing electrochemical stability.

Based on its unique structural evolution, 6H-$BaRuO_3$ after 50-cycle activation was selected for detailed HER evaluation. As shown in Figure 1a, activated 6H-$BaRuO_3$ consists of a bulk crystalline region (region I) and a weakly crystalline surface region (region II) indexed to RuO_2 with a 0.31 nm lattice spacing. fast fourier transform (FFT) patterns confirm the (104) planes of 6H-$BaRuO_3$ and partial amorphous features. EDS mapping further (Figure 1b) shows that the Ba-rich area (green dotted lines) is smaller than the Ru-rich area (white dotted lines), with surface Ba depletion evidenced by Ba (13.7%), Ru (27.9%), and O (58.4%) ratios. EDS line scans further verify reduced Ba content near the surface. Refined electron energy loss spectroscopy (EELS) spectra (Figure 1c) reveal electronic differences between the surface (areas 1–2) and bulk (area 3). The Ru *M*-edge in area 2 shifts by 1.3 eV toward lower energy, indicating a reduced Ru valence after LSV activation. Meanwhile, the O *K*-edge in area 2 exhibits a distinct feature associated with Ru 4*d*–O 2*p* hybridization [23], which is less pronounced in area 3. The weaker Ba *M*-edge signals further confirm surface Ba depletion.

The local coordination and oxidation state of Ru were further examined by synchrotron-based x-ray absorption spectroscopy (XAS). X-ray Absorption Near-Edge Structure (XANES) spectra (Figure 1d) show that the absorption edges of activated samples approach that of RuO_2, and calculated Ru valence states progressively decrease from +3.59 (first LSV) to +3.44 (35th

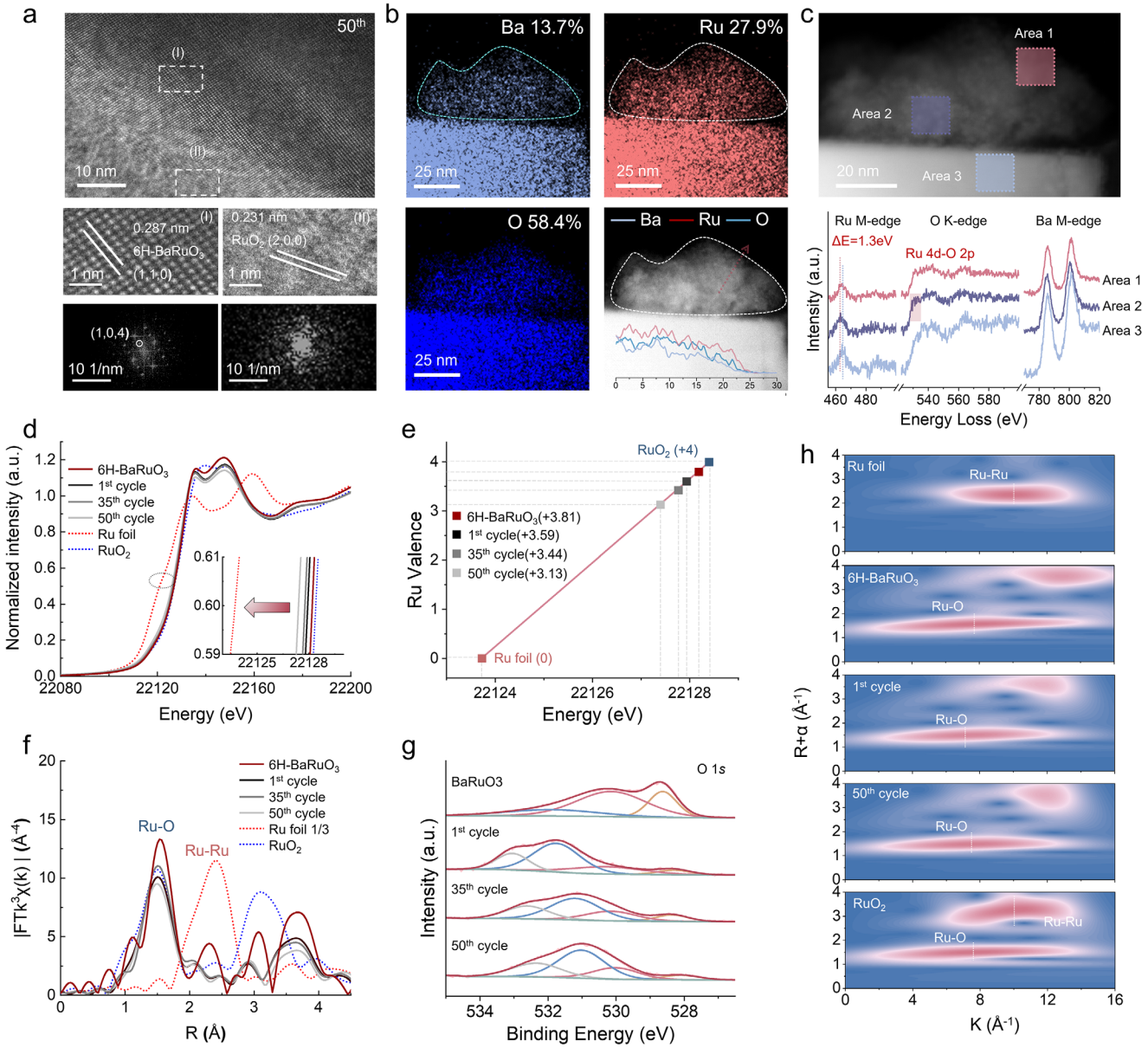

FIGURE 1 | Structural characterization of 6H-$BaRuO_3$ after LSV activations. (a) HR-TEM images with corresponding magnified regions and FFT patterns after 50-cycles. (b) HAADF image and elemental mapping with line-scan EDS profiles after 50-cycles. (c) HAADF images and corresponding EELS spectra after 50-cycles. (d) Ru *K*-edge XANES spectra. (e) Calculated Ru valence states. (f) Ru EXAFS spectra. (g) O 1 s XPS spectra. (h) WT analysis of EXAFS results.

LSV) and +3.13 (50th LSV) (Figure 1e). This trend correlates negatively with the HER performance discussed later. Fourier-transformed extended x-ray absorption fine structure (EXAFS, non-phase-shift corrected) in Figure 1f for the activated 6H-$BaRuO_3$ samples reveals a dominant Ru–O coordination shell at approximately 1.50 Å, shorter than that in pristine 6H-$BaRuO_3$ (1.53 Å), and the absence of Ru–Ru scattering at 2.41 Å (as observed in Ru foil), confirming Ru's changes in the local environment. The Ru–O coordination number decreases after the first cycle, increases slightly after the 35th cycle, and decreases again after the 50th cycle. This behavior reveals a dynamic evolution of surface reconstruction, likely arising from the equilibrium between oxygen vacancy formation in $BaRuO_3$ and the generation of surface Ru_xO_y species. X-ray photoelectron spectroscopy (XPS) of O 1s further provides insights into the surface oxygen species (Figure 1g). The pristine 6H-$BaRuO_3$ shows three peaks corresponding to lattice oxygen, adsorbed oxygen, and adsorbed H_2O at 528.65, 530.2, and 532.2 eV, respectively. After activation, new features attributed to O^-/O^{2-} species appear, particularly at 531.05 eV for the 50th LSV sample. The progressive shift of this peak toward lower binding energy from the first to the 50th LSV sample indicates strong charge redistribution through surface oxygen bridges during reconstruction. Interestingly, the proportion of oxygen vacancies in the O 1s spectrum increases to 52.1% after the first LSV cycle, decreases to 46.3% after the 35th cycle, and rises again to 48.8% after the 50th cycle. This observation further confirms that the reconstruction mainly occurs on the surface, as XPS is highly sensitive to surface chemistry. We refer that oxygen vacancies form on the $BaRuO_3$ surface after the initial cycle, followed by the generation of surface

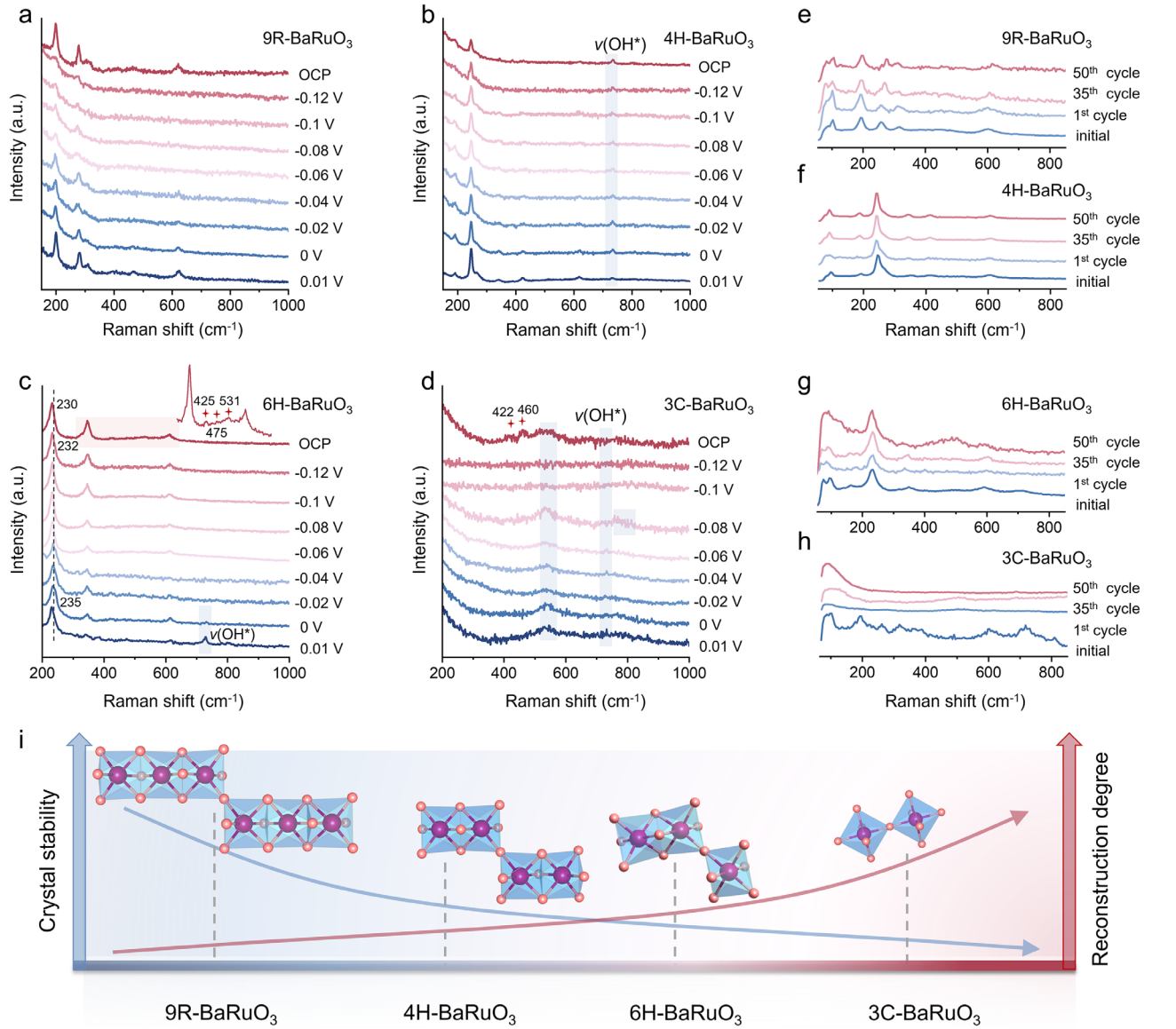

FIGURE 2 | Raman spectroscopy for $BaRuO_3$ family. (a–d) In situ Raman spectra of (a) 9R-$BaRuO_3$, (b) 4H-$BaRuO_3$, (c) 6H-$BaRuO_3$, and (d) 3C-$BaRuO_3$. (e–h) Ex situ Raman spectra of (e) 9R-$BaRuO_3$, (f) 4H-$BaRuO_3$, (g) 6H-$BaRuO_3$, and (h) 3C-$BaRuO_3$ after the first to 50th LSV cycles. (i) Schematic illustration of crystal stability and reconstruction degree.

Ru_xO_y and subsequent vacancy regeneration, which aligns well with the EXAFS and TEM results. Wavelet transform (WT) analysis of the EXAFS signals (Figure 1h) further confirms these structural changes. The characteristic signals at 7.52 and 12.05 $Å^{-1}$ for the 50th LSV sample correspond to Ru–O and Ru–Ru coordination, respectively, evidencing the formation of new local environments compared to the original 6H-$BaRuO_3$ structure (7.59 and 13.17 $Å^{-1}$).

2.2 | In situ Raman Analysts for Dynamic Mechanism

In situ Raman spectroscopy was first used to track how RuO_6 connectivity directs the pathway of surface reconstruction during HER. In situ Raman spectroscopy (0.01 to −0.12 V in 1 M KOH) was employed to monitor surface reconstruction and intermediate evolution during the HER process (Figure 2). For comparison, the pristine Raman spectra of 9R-, 4H-, 6H-, and 3C-$BaRuO_3$ are presented, and their peak positions are summarized alongside literature values in Figure S14. At 0.01 V, 9R-$BaRuO_3$ shows distinct peaks at 200, 281, 310, 465 and 623 cm^{-1} (Figure 2a), corresponding to the E_g (Ru vibrations in a-b plane), A_{1g} (Ru vibrations along out-of plane), E_g (O), A_{1g} (O) and A_{1g} (O) active modes [24], with negligible spectral changes as the potential becomes more negative. For 4H-$BaRuO_3$, seven characteristic peaks are identified (Figure 2b)—six at 191.1, 247, 265, 340.8, 422.7 and 619 cm^{-1} (E_{2g}(Ru), E_{2g}(O), A_{1g}(Ru), E_{2g}(O), E_{1g}(O), and A_{1g}(O) modes) and an additional band at 731 cm^{-1} assigned to adsorbed OH* [13]. Although its overall profile remains largely stable under cathodic bias, the Raman peak for OH* produced from water dissociation, gradually intensifies as the potential decreases. Normally, adsorbed OH* would desorb ($OH^* + e^- \rightarrow OH^-$), leading to a weaker signal; however, the sustained intensity suggests

continuous OH* replenishment via water dissociation. For 6H-$BaRuO_3$ in Figure 2c, the OH* adsorption peak (728 cm^{-1}) emerges at +0.01 V but vanishes by 0 V, indicating fast OH* desorption. As the potential is further lowered from 0 to −0.12 V, the main Ru–O band redshifts, implying partial Ru ions valence state reduction [13, 25]. Interestingly, when the applied potential reaches −0.10 V, a pronounced Raman peak emerges at 588 cm^{-1} and persists down to −0.12 V. According to the assignment reported by Jo et al., this feature can be attributed to the formation of Ru^{3+}—O bonds [26, 27], which is not distinctly observed in other $BaRuO_3$ polymorphs. Upon returning the potential to open-circuit potential (OCP), additional Raman peaks appear at 425, 475, and 531 cm^{-1}, which can be assigned to Ru–OH in $RuO_2{\cdot}xH_2O$, Ru-O in $RuO_2{\cdot}xH_2O$, and the E_g-mode Ru–O vibration in RuO_2, respectively [25, 26, 28, 29]. Notably, Jo et al. employed isotopic substitution experiments and demonstrated that the characteristic low-frequency peak shifts from 434 cm^{-1} in $RuO_2{\cdot}xH_2O$ to 422 cm^{-1} in $RuO_2{\cdot}xD_2O$ [26], thereby unambiguously confirming the involvement of Ru–OH vibrations in the in situ Raman spectra, which is in excellent agreement with our assignment. In contrast, 3C-$BaRuO_3$ displays broader bands at 520 cm^{-1} (Ru–O) and 710 cm^{-1} (adsorbed OH*) at +0.01 V in Figure 2d [30]. As the potential approaches −0.08 V, the OH* feature peak broadens, confirming that water dissociation continuously replenishes desorbed species. At –0.10 V, intense hydrogen bubbling obscures most peaks. Once the bias voltage is removed, sharper Raman bands reappear at 422 and 460 cm^{-1}, which can be assigned to the Ru–OH and Ru–O vibrations in $RuO_2{\cdot}xH_2O$, respectively. These features indicate a stronger coupling and interaction between Ru and H_2O, which are more pronounced than those observed in 6H-$BaRuO_3$, suggesting more extensive Ru–O surface reconstruction.

Ex situ Raman spectra recorded after 1, 35, and 50 LSV cycles further support these trends. The pristine 9R-$BaRuO_3$ (Figure 2e) and 4H-$BaRuO_3$ (Figure 2f) remain largely unchanged even after 50th cycles. In contrast, 6H-$BaRuO_3$ (Figure 2g) exhibits little spectral variation over the first 35 cycles but develops a broad band centered at ∼520 cm^{-1} after 50 cycles [29, 31], which can be tentatively assigned to the Ru–O vibration in RuO_2, accompanied by pronounced peak broadening indicative of amorphization. For 3C-$BaRuO_3$ (Figure 2h), this Ru–O feature appears after the first cycle and reaches maximum intensity by the 35th cycles, indicating rapid surface restructuring. After 50th cycles, most characteristic peaks disappear except for a broad Ba—O band around 90 cm^{-1}, suggesting severe structural degradation and extensive surface amorphization [24, 32]. Our results reveal a clear structure–activity correlation: an increasing fraction of corner-shared octahedra reduces the crystal stability and promotes surface reconstruction during the HER. This is manifested by the early emergence of Ru_xO_y species and partial reduction of Ru^{4+} on the 6H-$BaRuO_3$ and 3C-$BaRuO_3$ surfaces (0.01 to −0.12 V), accompanied by pronounced reconstruction after cycling, phenomena that are absent in the more stable 9R-$BaRuO_3$ and 4H-$BaRuO_3$ phases (Figure 2i). Moreover, the transient evolution of the OH* feature during reconstruction suggests that this process directly modulates the adsorption and desorption kinetics of reaction intermediates, as discussed below. The structural parameters, surface reconstruction characteristics, and dissolution behaviors of 9R-, 4H-, 6H-, and 3C-$BaRuO_3$ are summarized in Table S2, providing a basis for future AI (artificial intelligence)-assisted investigations into the structure–reconstruction correlations.

During alkaline HER, protons adsorbed on the Ru surface originate from bulk water molecules migrating to the interface through the hydrogen-bond network. This migration requires both dynamic reorganization of the network and rotational motion of water molecules, making in situ monitoring of adsorption and dissociation critical [33, 34]. To probe the origin of enhanced HER activity, we performed in situ Raman spectroscopy of interfacial water. As shown in Figure 3a–d, a broad O—H stretching band (3000–3800 cm^{-1}) appears, characteristic of interfacial water. Deconvolution resolves three Gaussian components at ∼3200, ∼3400, and ∼3600 cm^{-1}, corresponding to 4-coordinated hydrogen-bonded water (4HB-H_2O), 2-coordinated hydrogen-bonded water (2HB-H_2O), and weakly bound/free water (K^+-H_2O), respectively [35]. Free water molecules rotate easily but transfer protons inefficiently due to weak connectivity, whereas strongly hydrogen-bonded water forms a rigid network that demands higher reorientation energy for proton transfer. To better understand the interfacial water configuration, the distributions of 4HB-H_2O, 2HB-H_2O, and K^+-H_2O were analyzed across the applied voltage range (Figure 3e,f; Figures S15 and S16). For 9R-$BaRuO_3$, sweeping the potential from 0 to −0.15 V decreases 2HB-H_2O (46.58% → 43.39%) while increasing 4HB-H_2O (40.15% → 44.25%); K^+-H_2O remains nearly constant. 4H-$BaRuO_3$ shows a similar trend (Figure S15), indicating gradual conversion of 2HB-H_2O to 4HB-H_2O driven by cation accumulation. In contrast, 6H-$BaRuO_3$ and 3C-$BaRuO_3$ display more pronounced changes.

For 6H-$BaRuO_3$, K^+-H_2O first increases (12.48% → 16.40%) between 0 and −0.08 V due to facile adsorption, then slightly decreases (16.40% → 12.23%) from −0.08 to −0.15 V. Over the same range, 4HB-H_2O and 2HB-H_2O initially decrease (41.37% → 39.68% and 46.15% → 43.92%) and then increase and decrease (39.68% → 51.62% and 43.92% → 36.15%), respectively, suggesting a strengthening of the hydrogen-bond network. At the initial stage, cation-coordinated water accumulates at the interface, depleting hydrogen-bonded species. Subsequent restructuring consumes this layer, exposes active sites, facilitates O—H bond cleavage, and enhances product diffusion, likely due to in situ Ru_xO_y formation. 3C-$BaRuO_3$ exhibits non-monotonic three Gaussian peaks changes with a transition at −0.06 V (Figure S16), earlier than 6H-$BaRuO_3$, indicating a more reactive surface capable of reorganizing the hydrogen-bond network at milder potentials. Its OCP Raman spectra show a pronounced increase in strongly hydrogen-bonded water. Vibrational frequency shifts under applied potential reflect the Stark effect, highlighting intermediate sensitivity to the catalyst surface [36]. For 9R-$BaRuO_3$, all three O–H modes redshift significantly, whereas 4H-$BaRuO_3$ shows only minor changes. 6H-$BaRuO_3$ and 3C-$BaRuO_3$ switch from redshift to blueshift, indicating extensive interfacial reconstruction. The largest shifts are observed for 4HB-H_2O species, consistent with stronger interactions and closer proximity to the Ru_xO_y surface. Overall, surface reconstruction progressively reorganizes active sites, strengthens the interfacial hydrogen-bond network, and promotes water dissociation. This mechanism and its impact on alkaline HER are summarized in Figure 3g,i.

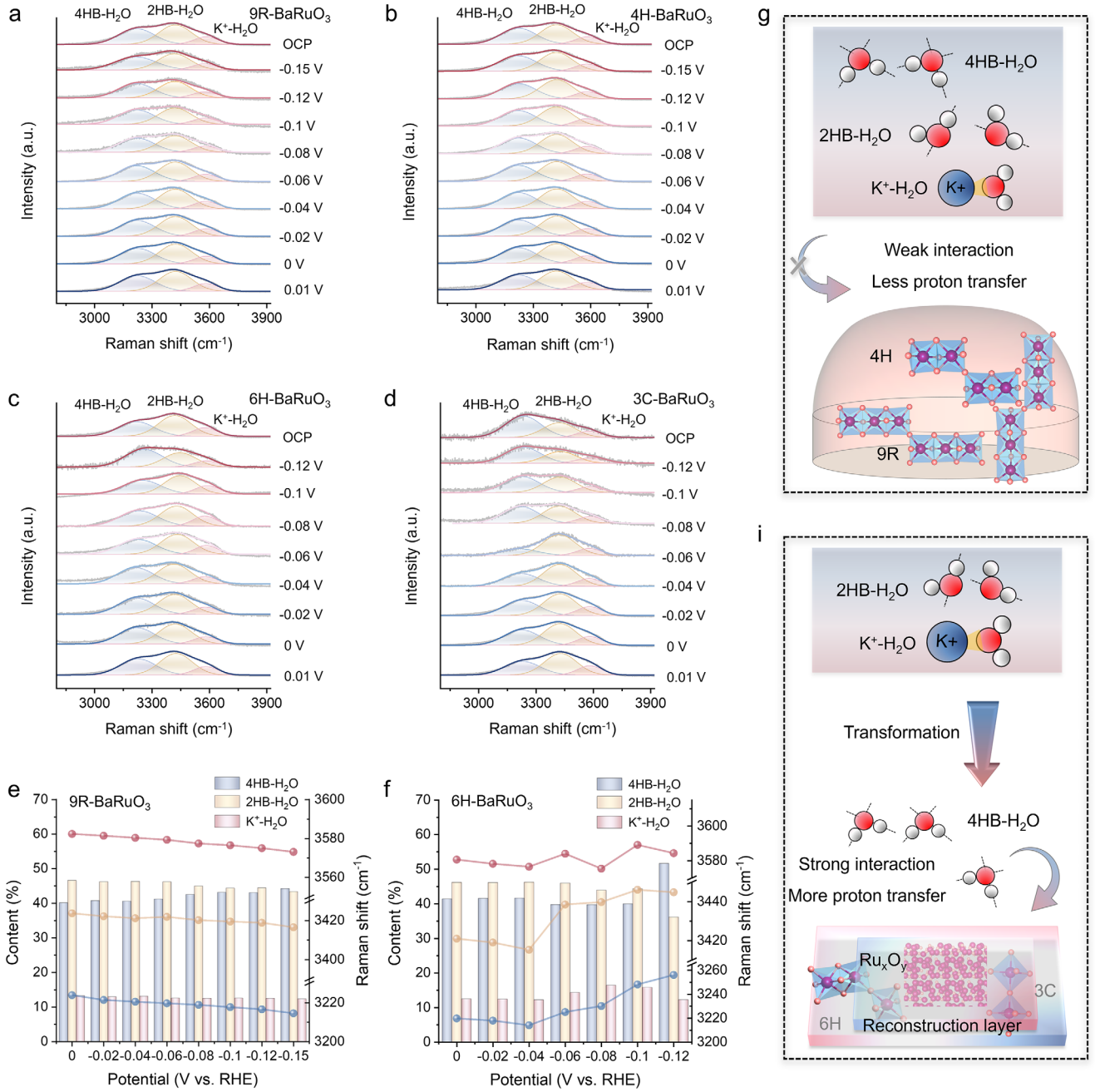

FIGURE 3 | Raman spectroscopic verification of the HER mechanism. (a–d) In situ Raman spectra of interfacial water for (a) 9R-$BaRuO_3$, (b) 4H-$BaRuO_3$, (c) 6H-$BaRuO_3$, and (d) 3C-$BaRuO_3$. (e,f) Peak area ratios of the three interfacial water structures and Stark tuning rates for (e) 9R-$BaRuO_3$ and (f) 6H-$BaRuO_3$. (g–i) Schematic illustrations showing the configurations of 4HB-H_2O, 2HB-H_2O, and K^+-H_2O at the (g) 9R-$BaRuO_3$, 4H-$BaRuO_3$ and (i) 6H-$BaRuO_3$, 3C-$BaRuO_3$ surfaces during HER.

2.3 | Excellent Electrocatalytic HER Performance

The HER performance of the catalysts was evaluated in a standard three-electrode setup in 1 M KOH. HER activity for $BaRuO_3$ family gradually improved with increasing LSV cycles, suggesting rapid surface reconstruction during HER (Figure S17). Electrochemical impedance spectroscopy (EIS) and double-layer capacitance (C_{dl}) measurements were performed before and after activation, revealing enhanced conductivity and electrochemically active surface area (ECSA) across all catalysts (Figures S18–S22 and Table S3), likely due to optimized surface structures. After 50 LSV cycles, 6H-$BaRuO_3$ showed the largest activity enhancement among the $BaRuO_3$ family (Figure 4a). Catalysts subjected to 50 cycles are denoted AC-9R, AC-4H, AC-6H, and AC-3C. AC-6H achieved an overpotential of just 11 mV at 10 mA cm^{-2}, outperforming AC-9R (45 mV), AC-4H (35 mV), AC-3C (29 mV), and commercial Pt/C (29 mV) (Figure 4b). It also exhibited the lowest Tafel slope of 27.4 mV dec^{-1} (Figure 4c), considerably smaller than AC-9R (80.1 mV dec^{-1}), AC-4H (71.6 mV $dec^{-1)}$, AC-3C (36.7 mV dec^{-1}), and Pt/C (32.6 mV dec^{-1}), indicating

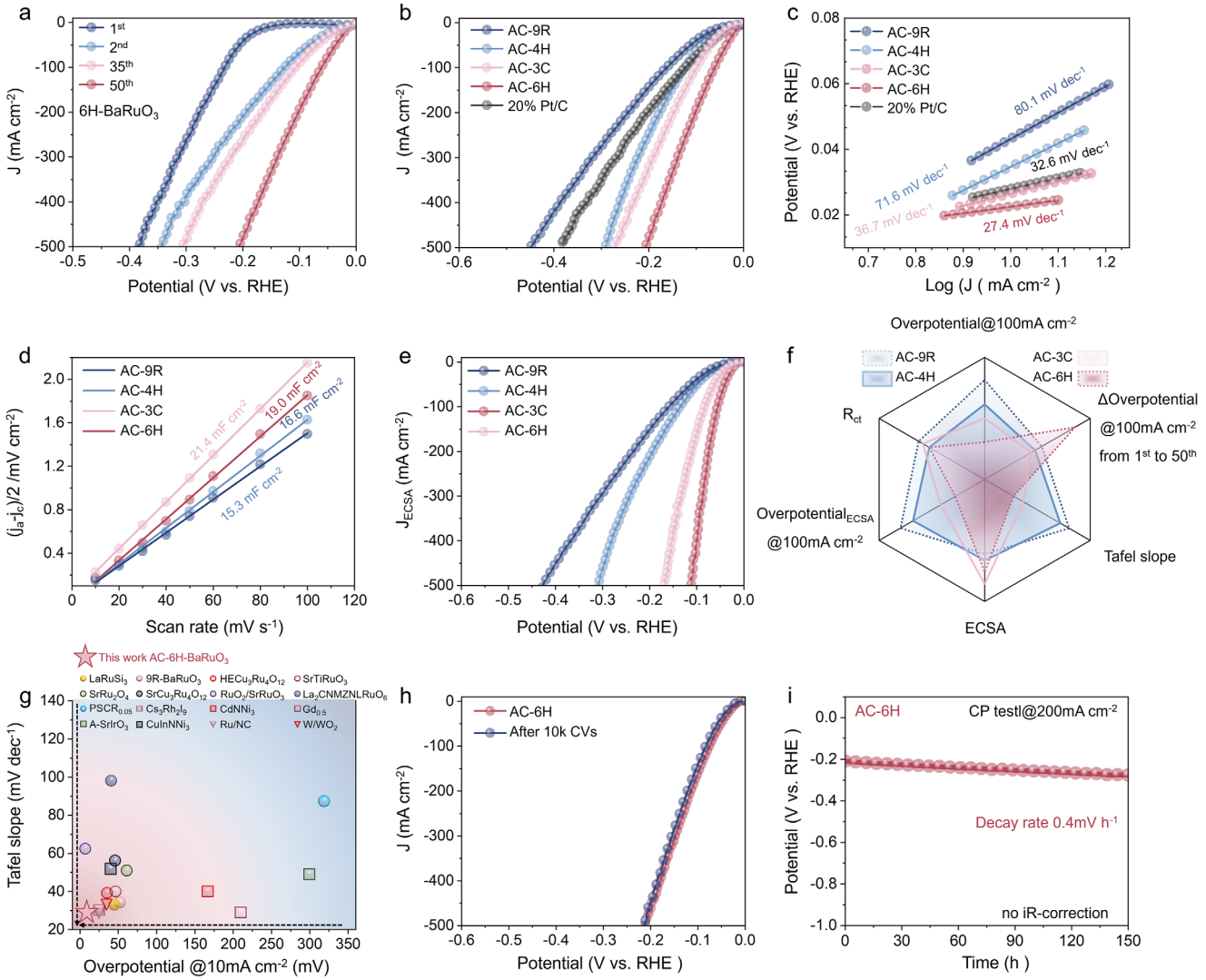

FIGURE 4 | Electrocatalytic HER performance in 1 M KOH. (a) Polarization curves for 6h-$BaRuO_3$ during different LSV cycles. (b) LSV curves. (c) Tafel plots. d) Current density (j) as a function of scan rate. (e) Specific activity normalized to ECSA. (f) Radar plot comparing performance metrics. (g) Alkaline HER activity comparison graph exhibiting the Tafel slope with η_{10}. (h) ADT tests. (i) CP test.

significantly faster HER kinetics. Electrochemically active surface area (ECSA) is widely used to evaluate electrocatalytic activity and is directly proportional to the electrochemical double-layer capacitance (C_{dl}) [37]. C_{dl} values for AC-9R, AC-4H, AC-6H, and AC-3C were measured at 15.3, 16.6, 19.0, and 21.4 mF cm^{-2}, respectively (Figure 4d). Notably, AC-3C exhibits the highest C_{dl} value, even exceeding that of AC-6H, which can be attributed to its unusually thick amorphous surface layer that provides more accessible active sites. After normalization by ECSA (Table S4), AC-6H demonstrated the highest intrinsic activity (Figure 4e). Radar analysis of performance (Figure 4f) shows progressive improvements in activity and kinetics with increasing corner-sharing octahedral order from AC-9R to AC-3C. AC-6H outperforms AC-3C, likely reflecting an optimal balance between surface reconstruction and structural stability, whereas excessive restructuring in AC-3C may reduce activity. Overall, the low overpotential and Tafel slope of AC-6H place it above many state-of-the-art perovskite catalysts reported in the literature (Figure 4g; Table S5).

Beyond catalytic activity, operational durability is a key metric for evaluating practical electrocatalysts [38]. As shown in Figure 4h, AC-6H retains nearly identical polarization curves during accelerated durability tests (ADTs) within the HER potential window, demonstrating excellent stability. Perovskite catalysts often deactivate under high current densities in alkaline HER, limiting industrial applicability. Impressively, AC-6H maintains a stable overpotential at −200 mA cm^{-2} for over 150 h during chronopotentiometry (CP) in Figure 4i, with a minimal decay rate of 0.4 mV h^{-1}. Post-150h-CP characterization using XRD, Raman, SEM, TEM, and ICP confirmed structural stability. No significant changes were observed in XRD patterns (Figure S23), indicating bulk integrity. Ex Raman spectroscopy shows that the broad Ru—O band near 500 cm^{-1} gradually disappears after a 150-h CP test (Figure S24), suggesting that the surface Ru_xO_y species may play a key role in the catalytic process. SEM and TEM images (Figure S25) show nearly unchanged morphology, while ICP analysis of the electrolyte revealed negligible Ru dissolution over time (Table S6). Taken together, AC-6H combines high

activity with exceptional stability, making 6H-$BaRuO_3$ a highly promising, tunable framework for practical alkaline electrolyzer applications, as demonstrated below.

To evaluate the practical applicability of 6H-$BaRuO_3$, a full-cell anion-exchange membrane water electrolyzer (AEMWE) was assembled (Figure S26), using 6H-$BaRuO_3$ as the cathode and FeNi-layered double hydroxides (LDH), a state-of-the-art oxygen evolution reaction (OER) material, as the anode [39]. Figure S26b,c shows polarization curves of AEMWEs operated at 60°C with 6H-$BaRuO_3$ and commercial Pt/C cathodes paired with FeNi-LDH anodes. The cell with 6H-$BaRuO_3$ reaches a current density of 1.0 A cm^{-2} at a lower voltage of 1.97 V, outperforming Pt/C at 2.07 V, highlighting its excellent device performance (Figure S26d). Importantly, a low hydrogen production cost of \$1.06 per kg H_2 is achieved at 1 A cm^{-2}, outperforming the Pt/C || FeNi-LDH benchmark (\$1.11 per kg H_2) in Figure S27, and approaching the department of energy (DOE) 2030 target (\$1.0 per kg H_2). Meanwhile, the 6H-$BaRuO_3$ cathode delivers remarkable durability at 500 mA cm^{-2} over 45 h, with an ultralow decay rate of 3.1 mV h^{-1}, substantially surpassing Pt/C (Figure S28) and underscoring its robustness under practical operating conditions.

2.4 | Theoretical Study on Electrocatalysis Mechanism

To elucidate the molecular origins of the enhanced catalytic activity of $Ru_xO_y/Ba_{1-\delta}RuO_{3-\delta}$ (denoted AC-6H, combining with Ru_xO_y and 6H), DFT calculations were carried out using interface models constructed from HR-TEM–derived orientations and Raman-resolved structural features (Figure 5a; Figure S29). These models integrate the (110) planes of 6H-$BaRuO_3$ with the (111) surfaces of a partially reduced amorphous Ru_xO_y layer and incorporate the oxygen and barium vacancies generated during dynamic reconstruction. For comparison, a $Ba_{1-\delta}RuO_{3-\delta}$ model (denoted 6H′) was constructed (Figure S30) instead of pristine 6H-$BaRuO_3$, because structural characterizations reveal that vacancies are generated immediately after the first LSV cycle, indicating that vacancy effects must be considered under realistic HER conditions. Since 9R-, 4H-, and 3C-$BaRuO_3$ undergo severe surface reconstruction and evolve into complex multiphase structures that have been partially investigated, we focus our DFT analysis on AC-6H to highlight its intrinsic catalytic mechanism.

Interfacial differential charge density mapping reveals pronounced electronic redistribution across the Ru_xO_y/6H junction (Figure 5b), consistent with strong coupling. Planar-averaged charge density profiles, together with Bader analysis confirm net electron transfer from 6H to Ru_xO_y regions (Figure 5c), indicating enhanced electronic delocalization across the interface. The Bader analysis further identifies a continuous charge gradient extending from the 6H region through the interface into the amorphous Ru_xO_y domains (Figure 5d). Ru atoms in the Ru_xO_y region exhibit the most pronounced charge loss (−1.62), while those at the interface and in the 6H region show progressively smaller losses (−1.35 and −1.28), confirming electron depletion at Ru sites within the reconstructed layer and charge migration through bridging O atoms. Oxygen species in Ru_xO_y display the highest effective oxidation state (+1.02), followed by O at the interface (+0.89) and O in 6H (+0.80), further supporting that amorphous Ru_xO_y serves as a highly effective electron reservoir that facilitates interfacial charge transfer during catalysis [40]. Recently, strong electronic coupling has been demonstrated at similar Ru/$BaRuO_3$ and RuO_2/$BaRuO_3$ heterointerfaces, where $BaRuO_3$ acts as an electron reservoir to establish a stable built-in electric field, in good agreement with our findings [22, 41]. In other words, Ru and O in the catalytic Ru_xO_y region undergo the greatest degree of charge transfer, which likely promotes stronger orbital hybridization. In AC-6H, the Ru–Ru (4f–4f) bond length is 2.46 Å, slightly contracted relative to 6H prime (2.55 Å), indicating compressive lattice strain induced by Ru_xO_y incorporation. Meanwhile, the Ru–Ru (4f–2a) distance in AC-6H decreases to 4.02 from 4.07 Å in 6H′, and the Ru_{2a}—O—Ru_{4f} bond angle likewise drops from 178.8° to 168.2°, a trend that correlates with strengthened orbital overlap and the formation of long-range, delocalized conduction channels in these triple perovskite structures.

Building on these structural features, the calculated density of states (DOS) indicates an increase in electronic states near the Fermi level following interface formation, suggesting improved conductivity that accelerates charge transfer and enhances HER performance (Figure 5e,f). In AC-6H, stronger hybridization between Ru 4*d* and O 2*p* orbitals near the Fermi level (EF) leads to more efficient 4*d*–2*p* electronic interactions, in agreement with Bader analysis, which facilitates faster interfacial charge transport. The adsorption of H* on Ru and O sites was probed using crystal orbital Hamilton population (COHP) analysis (Figure 5g,h), revealing the bonding and antibonding characteristics of Ru–H interactions. The electronic structure at specific sites, including the Ru 4*d*-band and O 2*p*-band, was analyzed using the projected density of states (Figure 5i). The Ru *d*-band center in AC-6H is located at −1.77 eV, slightly higher than in 6H′ (−1.82 eV), indicating a moderately stronger interaction with HER intermediates. Meanwhile, the O *p*-band broadens and contributes more to the hybridized states near EF, with its center shifted away from EF. These modifications indicate reinforced Ru–O coupling and orbital overlap, which adjust the adsorption energetics of intermediates and promote more efficient charge transfer at the interface. Quantitative analysis using integrated COHP (ICOHP) values shows that Ru–H and O–H interactions in AC-6H reach −1.16 and −3.97 eV, respectively, both more negative than in 6H′ (−0.71 and −3.77 eV) in Figure 5j. This reflects intrinsically stronger bonding and enhanced orbital overlap at the Ru and O active sites. The particularly more negative O–H ICOHP is likely due to vacancy-induced electronic unsaturation, which increases the H affinity of O sites, stabilizes adsorbed intermediates, and facilitates proton–electron transfer during HER [42]. These electronic features therefore directly link the reconstructed interface to improved catalytic behavior.

Previous Tafel slope analysis confirms that the AC-6H system follows a Volmer–Tafel mechanism in alkaline media. In this environment, the HER proceeds via two key steps: water dissociation and the formation of adsorbed hydrogen intermediates ($H_2O + e^- + * \rightarrow H^* + OH^-$), followed by hydrogen evolution ($H^* + e^- \rightarrow 1/2\ H_2$). Accordingly, highly active alkaline HER electrocatalysts must combine a low H_2O dissociation barrier with a moderate H binding energy, as rapid water dissociation is a prerequisite for efficient hydrogen evolution [43, 44].

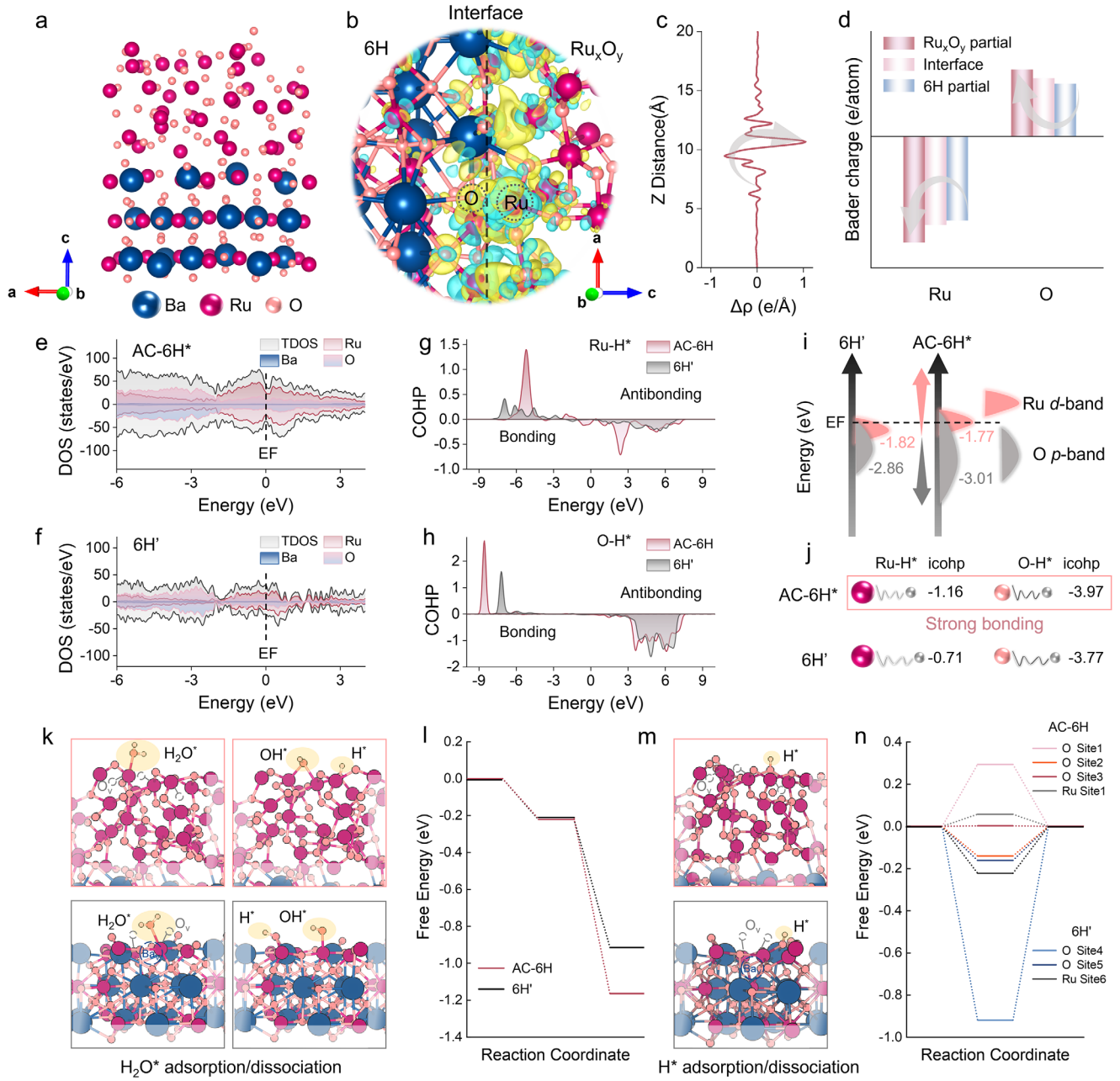

FIGURE 5 | DFT analysts for catalytic mechanism. (a) $Ru_xO_y/Ba_{1-\delta}RuO_{3-\delta}$ (AC-6H) DFT models (b) The differential charge density distributions for AC-6H. Yellow and cyan regions indicate electron accumulation and electron depletion, respectively. (c) The corresponding planar-average charge density plot. (d) Computed Bader charges of Ru and O atoms for Ru_xO_y, interface, and 6H regions. (e,f) The total DOS and projected DOS of Ba 4*d*, Ru 4*d*, and O 2*p* for AC-6H and 6H′. (g,h) The COHP for Ru–H* and O–H* of AC-6H and 6H′. (i,j) The schematic diagram of *d*-band center, *p*-band center, and COHP for AC-6H and 6H′. (k) The proposed HER mechanism for H_2O dissociation. The red box (top) represents AC-6H, and the black box (bottom) represents 6H′. (l) HER Gibbs free energy diagrams for H_2O dissociation. (m) The proposed HER mechanism for H* adsorption. (n) The Gibbs free energy diagrams for HER.

Remarkably, within the Ru-localized coordination environment on the Ru_xO_y surface (Figure 5k, top), water dissociation occurs via an essentially barrier-free pathway (Figure 5l). During this process, water molecules are adsorbed on Ru sites, generating OH* intermediates while the liberated H* species are stabilized at adjacent O sites (Figure S31). A similar mechanism is observed on 6H′ (Figure 5k, bottom). The computed H_2O adsorption energies for AC-6H and 6H′ are −0.22 and −0.21 eV, respectively, indicating substantially stronger water binding on AC-6H. In addition, the water dissociation energy barrier on AC-6H is −1.16 eV, lower than that of 6H′ (−0.91 eV), suggesting spontaneous reaction progression. Notably, upon water adsorption onto the Ru active sites, the H–O–H angle in AC-6H increases markedly from 105.9° to 106.3°, indicating a facilitated activation of water molecules compared to that in 6H′. The adsorption free energy of hydrogen intermediates (ΔG_{H^*}) serves as a key descriptor of HER activity. Calculations for AC-6H (Figure 5m,n; Figure S32) show ΔG_{H^*} values of 0.290 eV at O site1, −0.140 eV at O site2,

0.003 V at O site3, and 0.058 eV at Ru site1, whereas in 6H′, ΔG_{H^*} at O site4 (−0.92 eV), O site5 (−0.16 eV), and Ru site2 (−0.22 eV) indicates less favorable adsorption. Catalysts with positive ΔG_{H^*} bind H* too weakly, whereas excessively negative ΔG_{H^*} hinders H_2 release; the ideal value is close to zero. These results demonstrate that AC-6H provides energetically favorable hydrogen adsorption, with H* desorption primarily occurring at O sites rather than Ru sites. Overall, AC-6H exhibits lower adsorption/desorption barriers compared with 6H′, supporting superior HER kinetics. Collectively, these findings reveal that AC-6H combines facile water dissociation with optimized hydrogen adsorption/desorption energetics, which together promote efficient HER in alkaline media [45].

3 | Conclusion

In summary, this work demonstrates that tailoring the connectivity of RuO_6 octahedra provides an effective strategy for regulating structural reconstruction and enhancing alkaline HER performance in $BaRuO_3$ perovskites. By precisely tuning the balance between corner- and face-sharing units, the 6H phase is identified as the optimal configuration, achieving bulk structural stability while enabling self-activated surface reconstruction. The proportion of RuO_6 connectivity fundamentally governs the reconstruction pathway: increased corner-sharing weakens lattice cohesion and accelerates Ba/Ru dissolution with the formation of amorphous Ru_xO_y, whereas excessive face-sharing suppresses reconstruction. Owing to its balanced connectivity, the 6H phase undergoes moderate, well-regulated reconstruction that preserves bulk integrity while generating catalytically active amorphous Ru_xO_y domains. In situ Raman spectroscopy reveals the rapid formation of surface Ru_xO_y during HER, accompanied by dynamic intermediate turnover. DFT calculations show that the reconstructed Ru_xO_y domains drive substantial interfacial charge redistribution, strengthen Ru–O hybridization, lower the water-dissociation barrier, and optimize hydrogen-adsorption energetics, collectively enabling fast HER kinetics. Benefiting from these synergistic structural and electronic effects, the AC-6H heterostructure achieves an ultralow overpotential of 11 mV at 10 mA cm^{-2}, a Tafel slope of 27.4 mV dec^{-1} and excellent durability exceeding 150 h at 200 mA cm^{-2} in 1.0 M KOH. Collectively, this study establishes a mechanistic foundation for octahedral-connectivity engineering and positions HPHT synthesis as an enabling strategy for accessing metastable, high-entropy perovskite architectures, thereby guiding the rational design of durable, reconstruction-assisted electrocatalysts.

Acknowledgements

This study was supported financially by the National Key Research and Development Program of China (Grant No. 2023YFA1406000), the National Natural Science Foundation of China (Grant Nos. 22171283, 52472087 and 12474002), and the fund of State Key Laboratory of Information Photonics and Optical Communications (Beijing University of Posts and Telecommunications, P. R. China). We acknowledge support from the Max Planck-POSTECH-Hsinchu Center for Complex Phase Materials. We acknowledge SOLEIL for provision of synchrotron radiation facilities, and we would like to thank the assistance from SOLEIL beamline staff. We would like to thank Scientific Compass (www.shiyanjia.com) for the support of ICP test.

Conflicts of Interest

The authors declare no conflicts of interest.

Data Availability Statement

The data that support the findings of this study are available from the corresponding author upon reasonable request.

References

1. S. Das, P. Heasman, T. Ben, and S. Qiu, "Porous Organic Materials: Strategic Design and Structure–Function Correlation," *Chemical Reviews* 117 (2017): 1515–1563, https://doi.org/10.1021/acs.chemrev.6b00439.

2. C. Wei, Z. Feng, G. G. Scherer, J. Barber, Y. Shao-Horn, and Z. J. Xu, "Cations in Octahedral Sites: A Descriptor for Oxygen Electrocatalysis on Transition-Metal Spinels," *Advanced Materials* 29 (2017): 1606800, https://doi.org/10.1002/adma.201606800.

3. R. O. Moore and J. J. Gurney, "Pyroxene Solid Solution in Garnets Included in Diamond," *Nature* 318 (1985): 553–555, https://doi.org/10.1038/318553a0.

4. T. Yang, L. Gao, J. Lu, et al., "One-stone-for-two-birds Strategy to Attain Beyond 25% Perovskite Solar Cells," *Nature Communications* 14 (2023): 839, https://doi.org/10.1038/s41467-023-36229-1.

5. C.-Q. Jin, J.-S. Zhou, J. B. Goodenough, et al., "High-pressure Synthesis of the Cubic Perovskite $BaRuO_3$ and Evolution of Ferromagnetism in $ARuO_3$ (A = Ca, Sr, Ba) Ruthenates," *Proceedings of the National Academy of Sciences* 105 (2008): 7115–7119, https://doi.org/10.1073/pnas.0710928105.

6. C. Zhu, H. Tian, P. Tan, et al., "Ruthenate Perovskite With Face-Sharing Motifs for Alkaline Hydrogen Evolution," *Chem Catalysis* 4 (2024): 101132, https://doi.org/10.1016/j.checat.2024.101132.

7. N. Sun, Z. Zheng, Z. Lai, et al., "Augmented Electrochemical Oxygen Evolution by D–p Orbital Electron Coupling," *Advanced Materials* 36 (2024): 2404772, https://doi.org/10.1002/adma.202404772.

8. D. Guan, K. Zhang, Z. Hu, et al., "Exceptionally Robust Face-Sharing Motifs Enable Efficient and Durable Water Oxidation," *Advanced Materials* 33 (2021): 2103392, https://doi.org/10.1002/adma.202103392.

9. N. Du, C. Roy, R. Peach, M. Turnbull, S. Thiele, and C. Bock, "Anion-Exchange Membrane Water Electrolyzers," *Chemical Reviews* 122 (2022): 11830–11895, https://doi.org/10.1021/acs.chemrev.1c00854.

10. M. Klingenhof, H. Trzesniowski, S. Koch, et al., "High-Performance Anion-Exchange Membrane Water Electrolysers Using NiX (X = Fe, Co, Mn) Catalyst-Coated Membranes With Redox-Active Ni–O Ligands," *Nature Catalysis* 7 (2024): 1213–1222, https://doi.org/10.1038/s41929-024-01238-w.

11. G. Chen, T. Wang, J. Zhang, et al., "Accelerated Hydrogen Evolution Kinetics on NiFe-Layered Double Hydroxide Electrocatalysts by Tailoring Water Dissociation Active Sites," *Advanced Materials* 30 (2018): 1706279, https://doi.org/10.1002/adma.201706279.

12. H. Q. Fu, M. Zhou, P. F. Liu, et al., "Hydrogen Spillover-Bridged Volmer/Tafel Processes Enabling Ampere-Level Current Density Alkaline Hydrogen Evolution Reaction Under Low Overpotential," *Journal of the American Chemical Society* 144 (2022): 6028–6039, https://doi.org/10.1021/jacs.2c01094.

13. X. Chen, X.-T. Wang, J.-B. Le, et al., "Revealing the Role of Interfacial Water and Key Intermediates at Ruthenium Surfaces in the Alkaline Hydrogen Evolution Reaction," *Nature Communications* 14 (2023): 5289, https://doi.org/10.1038/s41467-023-41030-1.

14. Y. Zhu, H. A. Tahini, Z. Hu, et al., "Unusual Synergistic Effect in Layered Ruddlesden– Popper Oxide Enables Ultrafast Hydrogen Evolution," *Nature Communications* 10 (2019): 149, https://doi.org/10.1038/s41467-018-08117-6.

15. H. Wang, Y. Jiao, G. Zhang, et al., "Stabilizing Electron-Deficient Ru Nanoclusters via Strong Electronic Metal-Support Interaction for

Practical Anion-Exchange Membrane Electrolyzer," *Advanced Functional Materials* 35 (2025): 2418617, https://doi.org/10.1002/adfm.202418617.

16. J. Feng, X. Wang, and H. Pan, "In-Situ Reconstruction of Catalyst in Electrocatalysis," *Advanced Materials* 36 (2024): 2411688, https://doi.org/10.1002/adma.202411688.

17. F. Tao and M. Salmeron, "Surface Restructuring and Predictive Design of Heterogeneous Catalysts," *Science* 386 (2024): adq0102, https://doi.org/10.1126/science.adq0102.

18. J. G. Zhao, L. X. Yang, Y. Yu, et al., "Structural and Physical Properties of the 6H $BaRuO_3$ Polymorph Synthesized Under High Pressure," *Journal of Solid State Chemistry* 180 (2007): 2816–2823, https://doi.org/10.1016/j.jssc.2007.07.031.

19. N. Li, L. Cai, C. Wang, et al., "Identification of the Active-layer Structures for Acidic Oxygen Evolution From 9R-$BaIrO_3$ Electrocatalyst With Enhanced Iridium Mass Activity," *Journal of the American Chemical Society* 143 (2021): 18001–18009, https://doi.org/10.1021/jacs.1c04087.

20. H. Zhang, K. Song, Z. Lin, et al., "In Situ Reconstructed Ru Clusters on $LaRuSi_3$ With Enhanced Electrocatalytic Activity for Alkaline Hydrogen Evolution," *Advanced Functional Materials* 34 (2024): 2405897, https://doi.org/10.1002/adfm.202405897.

21. Q. Xiao, W. Yuan, L. Li, and T. Xu, "Fabrication and Characteristics of Composite Phase Change Material Based on $Ba(OH)_2 \cdot 8H_2O$ for Thermal Energy Storage," *Solar Energy Materials and Solar Cells* 179 (2018): 339–345, https://doi.org/10.1016/j.solmat.2017.12.032.

22. L. Wang, B. Li, M. Li, et al., "Rational Design and Dynamic Ru Exsolution Enables Active Heterostructures Surpassing Pt for Alkaline Hydrogen Evolution," *Journal of the American Chemical Society* 148 (2026): 3128–3138, https://doi.org/10.1021/jacs.5c16183.

23. E. Marelli, J. Gazquez, E. Poghosyan, et al., "Correlation Between Oxygen Vacancies and Oxygen Evolution Reaction Activity for a Model Electrode: $PrBaCo_2O_{5+\delta}$," *Angewandte Chemie International Edition* 60 (2021): 14609–14619, https://doi.org/10.1002/anie.202103151.

24. Y. S. Lee, T. W. Noh, J. H. Park, et al., "Temperature-dependent Raman Spectroscopy in $BaRuO_3$ Systems," *Physical Review B* 65 (2002): 235113, https://doi.org/10.1103/PhysRevB.65.235113.

25. X.-M. Lin, X.-T. Wang, Y.-L. Deng, et al., "In Situ Probe of the Hydrogen Oxidation Reaction Intermediates on PtRu a Bimetallic Catalyst Surface by Core–Shell Nanoparticle-Enhanced Raman Spectroscopy," *Nano Letters* 22 (2022): 5544–5552, https://doi.org/10.1021/acs.nanolett.2c01744.

26. H. C. Jo, K. M. Kim, H. Cheong, S.-H. Lee, and S. K. Deb, "In Situ Raman Spectroscopy of $RuO_2 \cdot xH_2O$," *Electrochemical and Solid-State Letters* 8 (2005): E39–E41, https://doi.org/10.1149/1.1865673.

27. J. Yang, C. Zhang, T. Zhou, et al., "Gradient Oxygen Vacancy Engineering of RuO_{2-x} for Efficient Acidic Water Oxidation," *Journal of Materials Chemistry A* 13 (2025): 15832–15840, https://doi.org/10.1039/d5ta01078k.

28. H. Yang, Y. Yang, and S. Zou, "Surface-Enhanced Raman Spectroscopic Evidence of Methanol Oxidation on Ruthenium Electrodes," *The Journal of Physical Chemistry B* 110 (2006): 17296–17301, https://doi.org/10.1021/jp063694s.

29. Y. M. Chen, A. Korotcov, H. P. Hsu, Y. S. Huang, and D. S. Tsai, "Raman Scattering Characterization of Well-aligned RuO_2 Nanocrystals Grown on Sapphire Substrates," *New Journal of Physics* 9 (2007): 130, https://doi.org/10.1088/1367-2630/9/5/130.

30. S. Y. Mar, C. S. Chen, Y. S. Huang, and K. K. Tiong, "Characterization of RuO_2 Thin Films by Raman Spectroscopy," *Applied Surface Science* 90 (1995): 497–504, https://doi.org/10.1016/0169-4332(95)00177-8.

31. A. V. Korotcov, Y.-S. Huang, K.-K. Tiong, and D.-S. Tsai, "Raman Scattering Characterization of Well-Aligned RuO_2 and IrO_2 Nanocrystals," *Journal of Raman Spectroscopy* 38 (2007): 737–749, https://doi.org/10.1002/jrs.1655.

32. J. Quilty, H. J. Trodahl, and A. Edgar, "Raman Spectroscopy of $BaRuO_3$," *Solid State Communications* 86 (1993): 369–371, https://doi.org/10.1016/0038-1098(93)90859-L.

33. D. Cao, P. Gao, Y. Shen, et al., "Fabricating Lattice-Confined Pt Single Atoms With High Electron-Deficient State for Alkali Hydrogen Evolution Under Industrial-Current Density," *Advanced Materials* 37 (2025): 2414138, https://doi.org/10.1002/adma.202414138.

34. W. Yan, Y. Mou, M. Li, et al., "C15-Phase Platinum-Lanthanide Intermetallics for Efficient Hydrogen Evolution: Identifying Lanthanide's Enhanced Mechanism," *Advanced Materials* 37 (2025): 2506936, https://doi.org/10.1002/adma.202506936.

35. T. Zhang, Q. Ye, Z. Han, et al., "Biaxial Strain Induced OH Engineer for Accelerating Alkaline Hydrogen Evolution," *Nature Communications* 15 (2024): 6508, https://doi.org/10.1038/s41467-024-50942-5.

36. Y.-H. Wang, S. Zheng, W.-M. Yang, et al., "In situ Raman Spectroscopy Reveals the Structure and Dissociation of Interfacial Water," *Nature* 600 (2021): 81–85, https://doi.org/10.1038/s41586-021-04068-z.

37. N. Sun, Z. Zheng, H. Liu, et al., "Electronegativity-Engineered Gradient Arrangement in High-Entropy Heterostructures for Efficient Oxygen Evolution," *Chem Catalysis* 6 (2026): 101636, https://doi.org/10.1016/j.checat.2025.101636.

38. N. Sun, W. Li, Y. Qin, et al., "Screening A-Site Ordered Quadruple Perovskites for Alkaline Hydrogen Evolution Reaction via Unifying Electronic Configuration Descriptor," *Chinese Physics B* 33 (2024): 128101, https://doi.org/10.1088/1674-1056/ad8074.

39. Y. Shi, L. Song, Y. Liu, et al., "Dual Cocatalytic Sites Synergize NiFe Layered Double Hydroxide to Boost Oxygen Evolution Reaction in Anion Exchange Membrane Water Electrolyzer," *Advanced Energy Materials* 14 (2024): 2402046, https://doi.org/10.1002/aenm.202402046.

40. N. Sun, Y. Qin, G. Xu, et al., "Manipulating Atomic Order-Disorder in Octahedral Building Blocks ($[MO_6]/[M_2O_9]$) for Advanced Hydrogen Evolution Electrocatalysis," *Applied Catalysis B: Environment and Energy* 383 (2026): 126107, https://doi.org/10.1016/j.apcatb.2025.126107.

41. Y. Yan, T. Meng, Y. Chen, et al., "Atomic-Level Coupled $RuO_2/BaRuO_3$ Heterostructure for Efficient Alkaline Hydrogen Evolution Reaction," *Journal of Energy Chemistry* 88 (2024): 356–362, https://doi.org/10.1016/j.jechem.2023.09.028.

42. K. Ji, S. Wang, S. Yao, et al., "Built-in Electric Field in Ru/CoP Bifunctional Electrocatalyst Enhances Hydrazine-Assisted Water Splitting," *Advanced Materials* 37 (2025): 2503182, https://doi.org/10.1002/adma.202503182.

43. Y. Chen, Z. Tang, Z. Liu, et al., "Toward the Ideal Alkaline Hydrogen Evolution Electrocatalyst: A Noble Metal-Free Antiperovskite Optimized With A-Site Tuning," *Advanced Materials* 37 (2025): 2504607, https://doi.org/10.1002/adma.202504607.

44. N. Sun, Z. Lai, W. Ding, et al., "Alkali Metals Activated High Entropy Double Perovskites for Boosted Hydrogen Evolution Reaction," *Advanced Science* 11 (2024): 2406453, https://doi.org/10.1002/advs.202406453.

45. J. Dai, Y. Zhu, H. A. Tahini, et al., "Single-phase Perovskite Oxide With Super-exchange Induced Atomic-Scale Synergistic Active Centers Enables Ultrafast Hydrogen Evolution," *Nature Communications* 11 (2020): 5657, https://doi.org/10.1038/s41467-020-19433-1.

Supporting Information

Additional supporting information can be found online in the Supporting Information section.

Supporting File: adfm75083-sup-0001-SuppMat.docx.